Enhancing directivity of terahertz photoconductive antennas using spoof surface plasmon structure

To cite this article before publication: Chi Wang *et al* 2022 *New J. Phys.* in press https://doi.org/10.1088/1367-2630/ac8116

Enhancing directivity of terahertz photoconductive antennas using spoof surface plasmon structure

Chi Wang[1,2], Zijian Zhang[1,2], Youfei Zhang[1],Xinrong Xie[1,2], Yumeng Yang[1,2], Jiaguang Han[3], Erping Li[1], Hongsheng Chen[1,2], Jianqiang Gu[3], Wei E.I. Sha[1*], Fei Gao[1,2,*]

[1] *Interdisciplinary Center for Quantum Information, State Key Laboratory of Modern Optical Instrumentation, College of Information Science and Electronic Engineering, Zhejiang University, Hangzhou 310027, China.*

[2] *International Joint Innovation Center, Zhejiang University, Haining 314400, China.*

[3]*Center for Terahertz Waves and College of Precision Instrument and Optoelectronics Engineering, Tianjin University, Tianjin 300072, China*

* Corresponding authors: E-mail: weisha@zju.edu.cn (W. E. I. Sha) gaofeizju@zju.edu.cn (F. Gao)

Keywords: metamaterials, spoof surface plasmons; terahertz

Abstract

Terahertz photoconductive antenna (PCA) is an important device for generating ultrabroadband terahertz radiations, being applicable in various scenarios. However, the metallic electrodes in PCAs, a pair of coplanar strip lines (CSL), always produce horizontal electrode modes in a broad THz band, thus resulting in low directivity in the vertical direction. Here, we introduce spoof surface plasmon polariton (SSPP) structures to suppress horizontal electrode modes in a broad band. The suppression principles are accounted to both the forbidden band of the fundamental SSPP mode and the orthogonality between source and higher-order SSPP modes. In the SSPP-modified PCA, we achieve around 2 dBi higher directivity in the vertical direction compared to a typical CSL PCA. Unlike

the narrow bands inheriting from conventional metamaterial resonators, the relative operational band of the SSPP-modified PCA is as broad as 48%. This planar SSPP structure is compatible with the well-developed micro fabrication technologies. Thus, our scheme can be combined with the semiconductor material engineering and plasmonic nanoscale structures for further increasing THz output power.

Introduction

Terahertz photoconductive antenna (PCA)[1, 2] is an important device for generating ultrabroadband THz radiations, which show important applications in next-generation wireless communications [3, 4], non-ionized imaging [5] , non-destructive detections [6], and spectroscopic analysis [7, 8]. The general principle of PCAs is that the picosecond carriers excited by femtosecond laser are driven by the biased voltages to generate THz radiations. **Figure 1(a)** is a typical PCA, whose horizontal and vertical directions are along *x*- and *z*-axis respectively. The vertical radiation of the PCA is usually harnessed for various applications. However, applications of THz PCAs are hindered by their low output efficiencies. The low-output issue originates from two reasons, including the low optical-to-THz conversion efficiency and low vertical directivity induced by horizontal electrode modes in PCAs.

Until now, much effort has been devoted to increasing the output

efficiencies of PCAs. To address the output issues, nanoscale structures[9-22], the choice of semiconductor photoconductive materials via strain-coupled heterostructures[23-25] and using the Ge/Rh-doped substrates[26], have been introduced into PCAs. However, these schemes only increase optical-to-THz conversion efficiency, but are incapable to eliminate electrode modes in PCAs. Especially, the metallic electrodes, a pair of coplanar strip lines (CSL), always lead to transmission-line (TL) electrode modes in a broad THz band. The horizonal modes further result in the reduction of vertical directivity of THz PCAs. Integrating microscale metamaterial resonators with PCAs provide feasible routes to suppress the TL electrode modes at specific frequencies, thus increasing directivities of PCAs in narrow bands [27-32].

Here, we propose a scheme to increase the directivity of PCAs in a broad band, by incorporating spoof surface plasmon polariton (SSPP)[33-35] structures in PCAs. The SSPP structure is a subwavelength metallic grating, which can host surface electromagnetic (EM) modes, analogous to surface plasmon polariton (SPP) in nano optics [36-38]. Different from the circuit-modeling scheme[39] improving output powers at specific frequencies, the SSPP-modified electrode can enhance directivity of the PCA antenna in a band of relative width 48%, and simultaneously achieve around 2 dBi higher directivity in the vertical direction than that of a typical CSL. This design allows for applying THz PCAs to sensing, imaging, and

detections.

Results

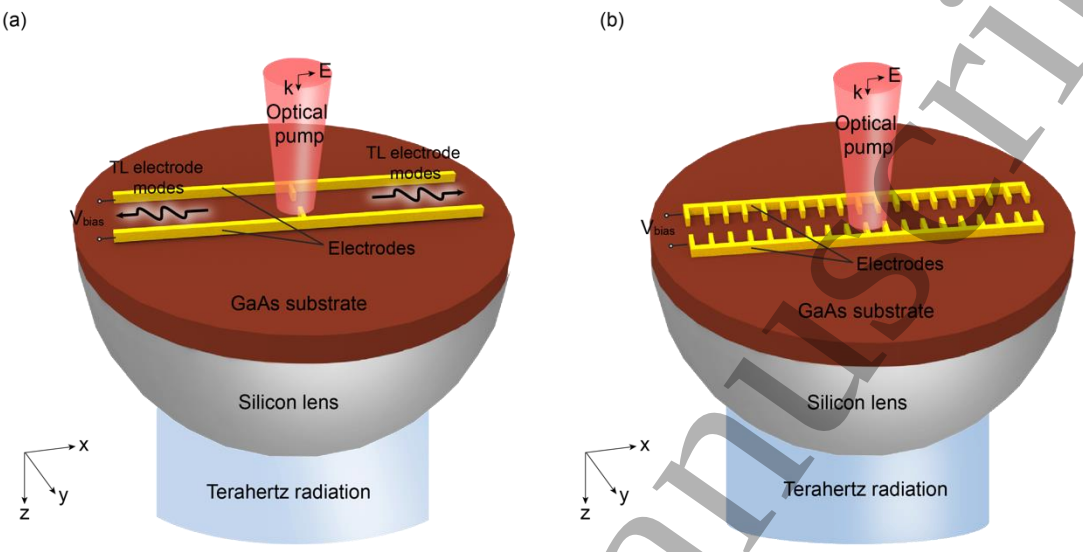

Figure 1 | Schematic of a terahertz SSPP-modified PCA. (a) a typical CSL photoconductive antenna (PCA), and **(b)** a spoof surface plasmon polariton (SSPP)-modified PCA.

Figure 1 shows the schematic diagrams of a typical CSL and a SSPP-modified PCAs. The typical PCA in **Fig. 1(a)** shows a CSL gold structure patterned on a gallium arsenide (GaAs) substrate. The terahertz radiation is generated at the center of the CSL structure, and collimated along the vertical (+*z*) direction by a silicon lens. However, partial THz waves could be guided along the CSL and form TL modes, which can travel horizontally, thus reducing the THz emission along the vertical (+*z*) direction. To address

the issue of horizontal electrode modes, we propose a SSPP-modified electrode as shown in **Figure 1(b)**. The SSPP structure is composed of periodic metallic grooves, which has been intensively utilized to guide surface electromagnetic waves [33].

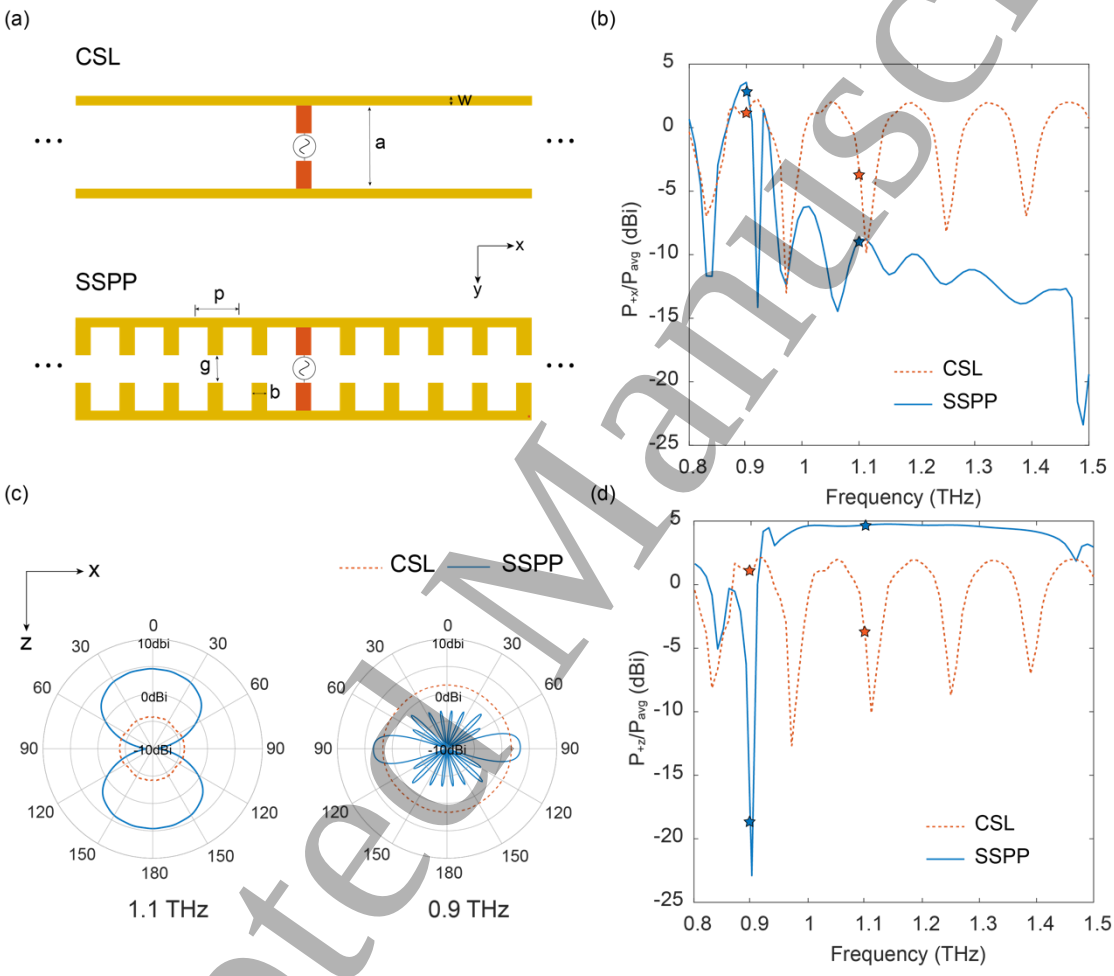

Figure 2 | The comparison between a freestanding CSL and SSPP-modified antenna. (a) The structures of a typical CSL antenna and a SSPP-modified antenna. Both PCAs share the same parallel metallic strips with width w = 10 μm, separated by distance a = 90 μm. In the SSPP-modified PCA, parallel metallic strips are decorated with periodic metallic

patches with period p = 105 μm, width b = 15 μm, and gap g = 15 μm. **(b)** The P_{+x} / P_{avg} of both antennas. **(c)** The radiation patterns in the *x*-*z* plane of both antennas at 0.9 THz and 1.1 THz, respectively. **(d)** The directivities of both antennas. The dashed and solid lines represent results of CSL and SSPP-modified antenna respectively.

To further quantify the advantages of the SSPP-modified electrode, we firstly compared the radiations from both CSL and SSPP-modified antennas without substrate. Both structures are illustrated in **Figure 2(a)**. They share the same parallel metallic CSL with a set of typical parameters, as length l = 2115 μm, width w = 10 μm, and separated by distance a = 90 μm. The parallel metallic strips in SSPP PCA are decorated by periodic metallic patches with period p = 105 μm, width b = 15 μm, and gap g = 15 μm. The thickness along the *z*-direction of the patches is 0.2 μm. We numerically explore the radiation performances by utilizing time-domain solver of CST Microwave Studio. In simulations, dipole sources in THz range are connected to the two metallic patches at the center of the CSL, to represent the photogenerated currents in PCAs. The boundary condition is open (add space). We employ directivity[40] $D = \max(P_{(\theta,\phi)})/P_{avg}$ to characterize the performance of PCAs, where $P_{(\theta,\phi)}$ and $P_{avg} = \frac{\int_{\theta=0}^{\pi}\int_{\phi=0}^{2\pi} P(\theta,\phi)\sin\theta d\theta d\phi}{4\pi}$ represent the radiation power in unit solid angle and average radiation power respectively. Since the CSL are along the

horizonal (x) directions (as shown in **Figure 2(a)**), their traveling TL modes result in the horizontal leakage with power P_{+x}. By simulation, we find that the SSPP-modified antenna shows lower P_{+x}/P_{avg} than that of the CSL one in 0.93-1.5 THz. The radiation patterns at 0.9 and 1.1 THz (shown in **Figure 2(c)**) further verify that the SSPP electrode can suppress the horizontal leakage, which exist in CSL ones. Simultaneously, the vertical radiations have been increased at least 3 dBi (**Figure 2(d)**). Since both antennas show z-mirror symmetry, the radiations along $\pm z$ directions are the same.

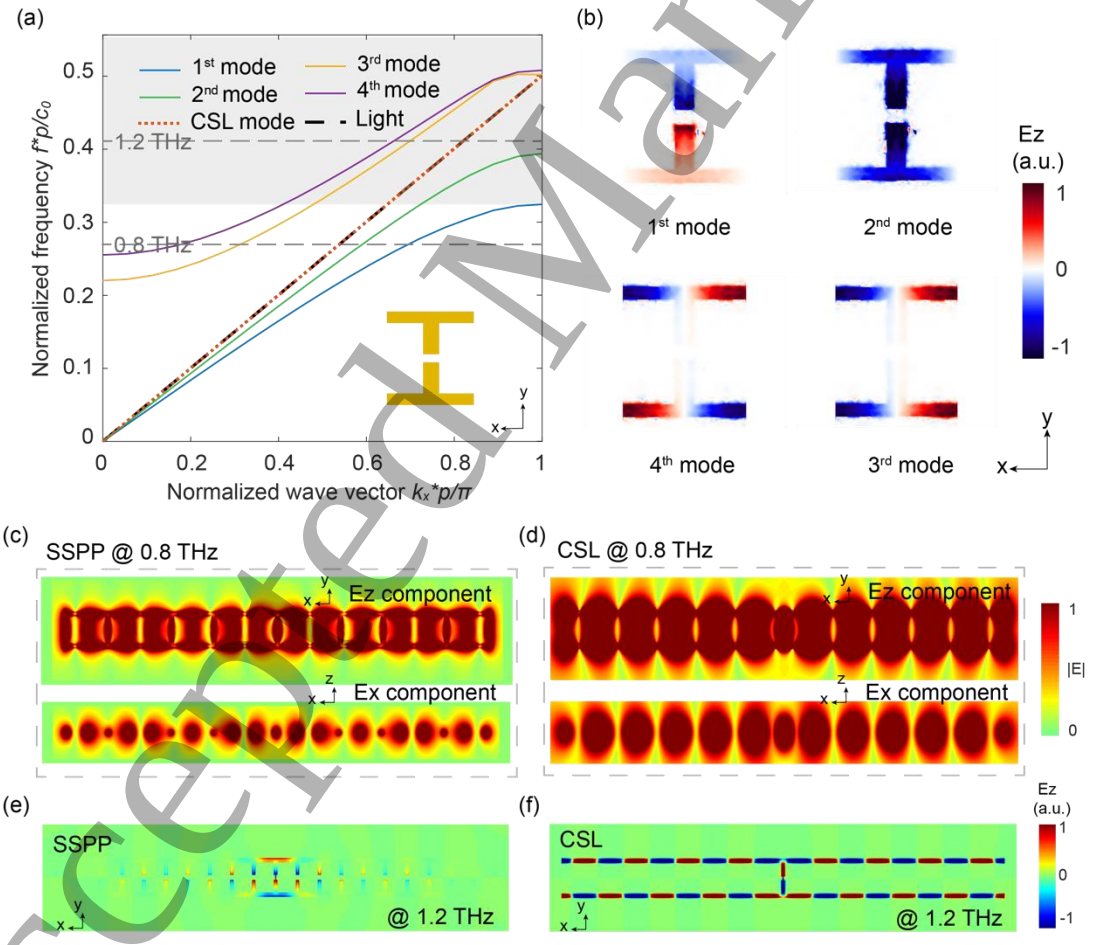

Figure 3 | The principle of suppressing the electrode modes in SSPP-modified PCAs. (a) The simulated dispersion relations of the CSL (red

dotted line), light line (black dotted) SSPP structure (solid lines). The inset shows the unit cell. The dashed line denotes corresponding eigenmodes at 1.0 THz. **(b)** E_z components for 1st, 2nd, 3rd, and 4th eigenmodes respectively. **(c-d)** The field amplitude excited in the SSPP-modified(c) and the CSL(d) antennas at 0.8 THz. **(e-f)** The *Ez* components excited in the SSPP-modified(e) and the CSL(f) antennas at 1.2 THz.

We then disclose that horizonal leakages are produced by the electrode modes. Here, we analyze the dispersion relations and eigenmode distributions by utilizing CST Microwave Studio. The backgrounds are 1600 μm along the *y* directions, and 200 μm along the *z* directions. The boundary conditions are periodic along the *x* direction, and perfect electric conductors along the *y* and *z* directions. We further show the simulated field patterns of the 3rd and 4th modes on the *x*-*y* (**Figure S1(c-d)** in SI) and *y*-*z* planes (**Figure S1(g-h)** in SI). Obviously, the dominated components (E_z and E_y) are well confined around the SSPP structure. It indicates both the 3rd and 4th modes originate from the SSPP structure, instead of the waveguide modes induced by the boundaries of the background box. However, their dispersions, lying above the light line (shown in **Figure 3(a)**), implies their leaky-wave natures. In **Figure 3(a)**, the dispersion of the CSL is a straight line without cutoffs, which supports broadband traveling or leaky TL modes. By integrating the SSPP structures, the

modified electrode supports four SSPP modes (shown in **Figure 3(a)**), instead of the leaky TL modes. Interestingly, none SSPP mode is excited by the y-polarized dipole in the broad band from 0.93 to 1.5 THz. This band is forbidden for the 1st eigenmode, whose cutoff frequency is 0.93 THz. Although 2nd, 3rd and 4th eigenmodes of SSPP all reside in between 0.93-1.5 THz, they cannot be efficiently excited by the dipole source located in the gap. We utilize the excitation efficiency[41] $\eta_i = \int \boldsymbol{E_d}^*(\boldsymbol{x},\boldsymbol{y},\boldsymbol{z}) \cdot \boldsymbol{E_{ei}}(\boldsymbol{x},\boldsymbol{y},\boldsymbol{z})\boldsymbol{dxdydz}$ for explanation, where i represents the i^{th} eigenmode, $\mathbf{E}_d$ and $\mathbf{E}_{ei}$ represent the normalized excitation field of the dipole and the i^{th} normalized eigenmode field of the SSPP structure, respectively. Along the y direction, the 2nd eigenmode shown in **Figure 3(b)** exhibits even parity, orthogonal to the mode of the dipole source with y-odd parity. Similarly, both excitation efficiencies of 3rd and 4th eignmodes are vanished, since their odd parities along the x direction are incompatible with the x-even parity of the dipole source. Compared with the near-field patterns of CSL at 0.8 THz (as shown in **Figure 3(d)**), the SSPP mode propagates along the x direction and the fields are confined along both the y and z directions (as shown in **Figure 3(c)**). The excited near-field patterns at 1.2THz (as shown in **Figure 3(e-f)**) further demonstrate the results of suppressing SSPP electrode modes. From the symmetries of the excited SSPP mode shown in **Figure 3(e)**, we can tell that the mode pattern at 1.2 THz only belongs to 1st eigenmode, whose propagation is forbidden along the x direction. It is

because that 1.2 THz falls into the band gap of 1st eigenmode. In contrast, the TL modes can propagate along the CSL (Fig. 3f), and induce horizontal leakages.

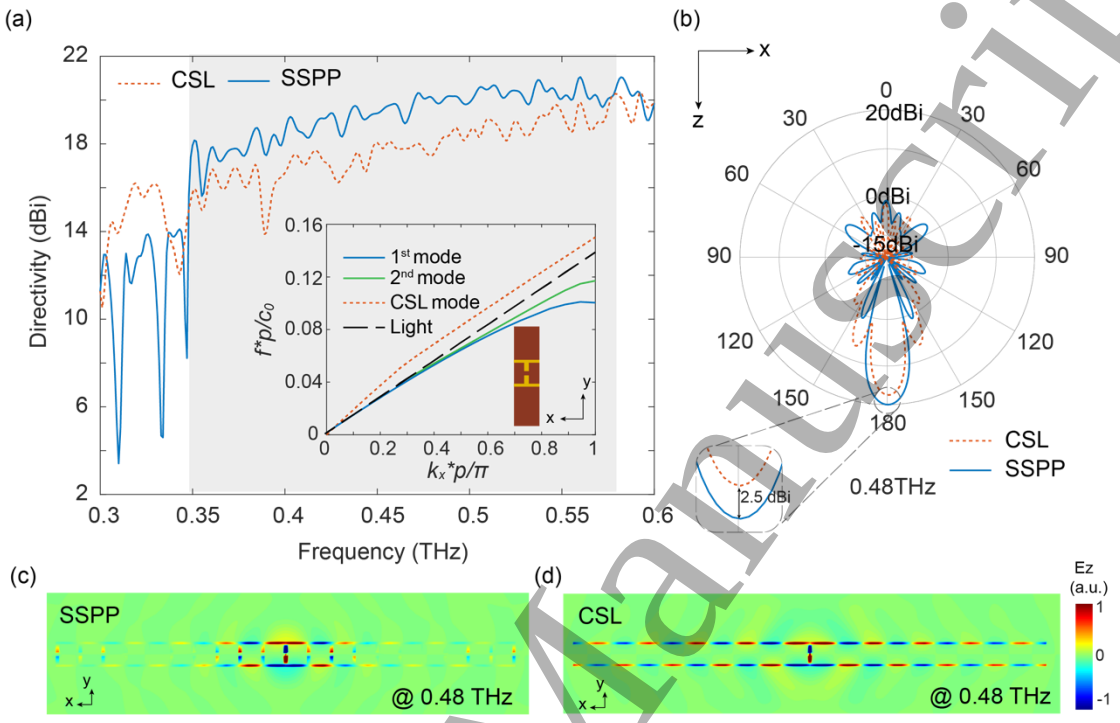

Figure 4 | The directivity of substrate-integrated SSPP-modified antenna with silicon lens. (a) The directivities of substrate-integrated CSL (red dashed line) and SSPP (blue solid line) antennas with silicon lens. The inset shows both the dispersion relations of the substrate-integrated CSL, the light line, the 1st and 2nd eigenmodes of substrate-integrated SSPP structure, whose corresponding unit cell is also shown in the inset. **(b)** The radiation patterns in *x*-*z* plane of both antennas at 0.48 THz. **(c-d)** The near-field patterns excited at 0.48 THz in the substrate-integrated SSPP (c) and the substrate-integrated CSL antennas (d), respectively.

The theoretical analysis above can also be applied in the practical PCA integrated with substrates. We model the GaAs substrate as a 473.7 μm-thick slab with the relative permittivity $\varepsilon_{GaAs} = 12.94$. A silicon lens ($\varepsilon_{Si} = 11.9$) is also integrated for increasing the directivity of PCAs and modeled as a semi sphere with the radius of 1160 μm, whose focus is set at the location of dipole sources. Both metallic structures remain the same as above. Integrating with the substrate and lens, the SSPP-modified antenna still shows about 2 dBi higher directivity (in **Figure 4(a)**) than that of the CSL. Due to the high permittivity of the substrate, the operational bandwidth is downshifted to the frequency range from 0.35 to 0.57 THz, which is consistent with the cutoff frequency of 1st eigenmode as depicted in the inset of **Figure 4(a)**. In contrast to the freestanding antennas, the radiation pattern (as shown in **Figure 4(b)**) of substrate-integrated SSPP antenna does not show remarkable suppression of the horizontal leakages. The phenomenon of the similar horizontal leakages is because that the leaky TL modes in CSL are not allowed to radiate into ambient efficiently, rather than the disfunction of SSPP structures. The low outcoupling of TL modes is accounted to the impedance mismatching between the air and the high-permittivity substrate, which highly confines the THz waves. The substrate confinement is also verified with the drastic reduction of -*z*-direction radiation. The near-field patterns in **Figure 4(c-d)** show that the substrate-integrated SSPP structures can still suppress the horizontal SSPP

electrode modes, consistent with above freestanding case.

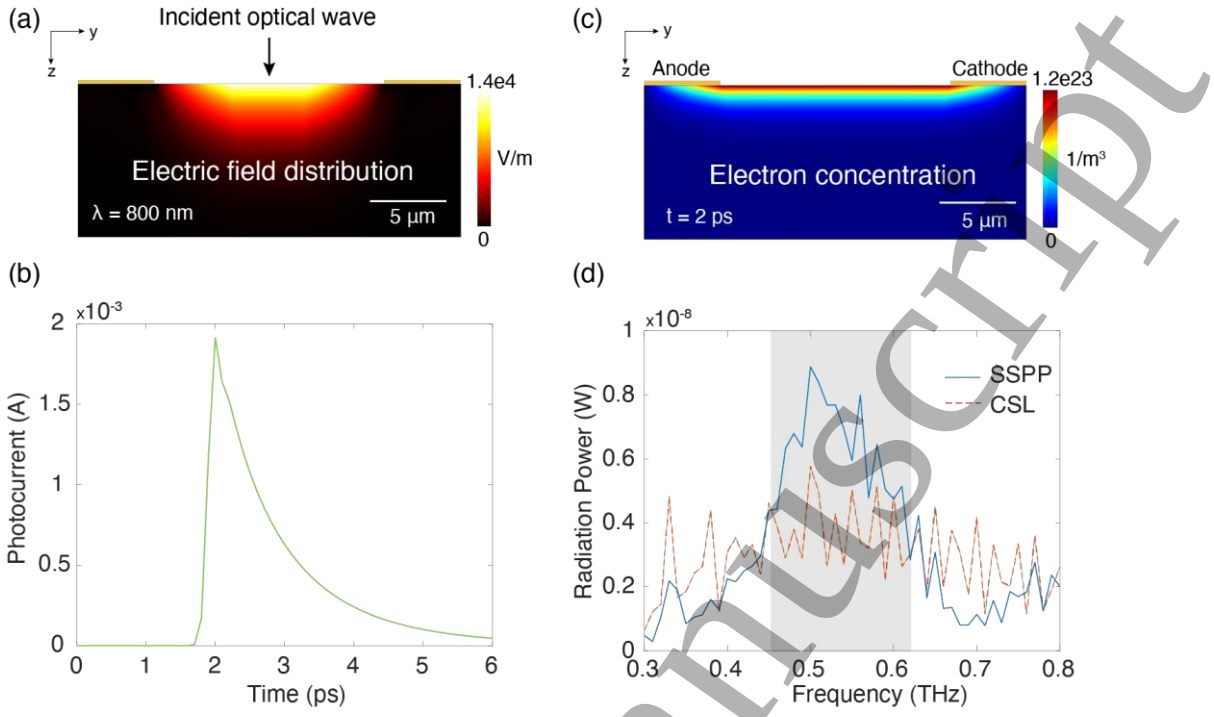

Figure 5 | The process of optical-to-THz conversion. (a) The electric field distribution of the cross-section in GaAs substrate due to an incident optical wave ($\lambda = 800$ nm). **(b)** The induced photocurrent in response to an optical pump pulse. **(c)** The electron concentration on the cross section of the substrate at 2 ps. **(d)** The comparison of the radiation power between the SSPP-modified PCA and the typical PCA.

For further demonstrating the performance of SSPP-PCA, we replace the excitation of dipole source with the practical photo-generated current. The optical-to-THz conversion process consists of two steps, including photocurrent generation excited by a femtosecond optical pulse, and terahertz generation from the PCA. We numerically studied the two steps

with COMSOL Multiphysics and CST respectively, where Maxwell's equations and drift-diffusion model are solved simultaneously. Regarding the first step, the optical pulse penetrating the GaAs, generates carriers, and then the electric field strength (E = 1.33 V/μm) drives the carriers to drift along the y direction, thus forming the photocurrent. We numerically study this process with a two-dimensional model, whose simulation area is 10 μm*25 μm on the y-z cross-section. The femtosecond optical pulse follows the gaussian shape, whose temporal center and width are 2 ps and 133 fs respectively. The optical pulses also have a spatial gaussian distribution along the y direction, whose half-power beam width (HPBW) is 2 μm. Taking the center wavelength λ = 800 nm of the pulse, we show its optical field spatial distribution on the GaAs substrate in **Figure 5(a)**. Driven by the electric field strength E = 1.33 V/μm, the photo-generated carriers form transient photocurrent $I_{comsol}(t)$ as depicted in **Figure 5(b)**, which quickly decays in several picoseconds. Taking the peak photocurrent at 2 ps, we show the electron spatial concentration in **Figure 5(c)**, which is consistent with the field distribution in **Figure 5(a)**. To numerically study the second step, we decompose the obtained transient current into Fourier components, whose coefficients are $A(f) = \int I_{comsol}(t)e^{-i2\pi ft}dt$. The spectral response of the SSPP-PCA that is a 3D geometry is simulated in CST. The output radiation power $P_{THz}(f)$ is shown in **Figure 5(d)**, which is proportional to the input current $I(f)$. Compared with the typical PCA, the

radiation power of the SSPP-modified PCA increases around 2dB in the band 0.45-0.62 THz. We further obtain the total output radiation power with $\int A(f)P_{THz}(f)df$. The optical-to-THz conversion efficiencies of the SSPP-modified PCAs are estimated to be 8.26E-5.

The major parameters of optical and electrical properties in the simulation are shown in Table 1 (the other details in SI section E):

Table 1. Optical and electrical properties

Symbol	Description	Unit	Value
λ	Free-space wavelength	nm	800
P	Incident power	μW	10
t_0	Pulse center location	ps	3
D_y	Pulse HPBW	μm	2
D_t	Pulse FWHM	fs	133
E	The electric field strength	V/μm	1.33
ε_{GaAs}	GaAs	None	12.94
k_{PC}	Photoconductor extinction coefficient of GaAs	None	0.0625

Conclusion

In summary, we propose a SSPP-modified electrode for increasing the directivity of THz PCAs. The underlying principle is suppressing the horizontal SSPP electrode modes. Compared with the conventional CSL PCA, we numerically demonstrate that the directivity of SSPP-modified one is increased around 2 dBi. Since the SSPP-modified electrode is planar, it is compatible the well-developed micro fabrication technologies. Meanwhile, the microscale SSPP structure could be combined with the nanoscale metamaterial structures[9-22] which may increase photocarrier concentration for further increasing the THz output power. Our proposal

could enable rich applications in high-performance terahertz sources.

Acknowledgements

This work was supported by National Natural Science Foundation of China (NNSFC) under Grants No. 62171406, 61801426, No.11961141010, ZJNSF under Grant No. Z20F010018, National Key Laboratory Foundation No. 6142205200402, and the Fundamental Research Funds for the Central Universities No. 2020XZZX002-15.

Competing interest

The authors declare no competing interests.

Data availability

The data that support the findings of this study are available from the corresponding author upon reasonable request.

Reference

1. D. H. Auston, K. P. Cheung, and P. R. Smith, "Picosecond photoconducting Hertzian dipoles," Applied Physics Letters **45**, 284-286 (1984).
2. M. B. Ketchen, D. Grischkowsky, T. C. Chen, C. C. Chi, I. N. Duling, N. J. Halas, J. M. Halbout, J. A. Kash, and G. P. Li, "Generation of subpicosecond electrical pulses on coplanar transmission lines," Applied Physics Letters **48**, 751-753 (1986).
3. T. Nagatsuma, G. Ducournau, and C. C. Renaud, "Advances in terahertz communications accelerated by photonics," Nature Photonics **10**, 371-379 (2016).
4. H. Sarieddeen, N. Saeed, T. Y. Al-Naffouri, and M.-S. Alouini, "Next generation terahertz communications: a rendezvous of sensing, imaging, and localization," IEEE Communications Magazine **58**, 69-75 (2020).
5. D. M. Mittleman, "Twenty years of terahertz imaging [Invited]," Opt Express **26**, 9417-9431 (2018).
6. K. Kawase, Y. Ogawa, and Y. Watanabe, "Non-destructive terahertz imaging of illicit drugs using spectral fingerprints," Optics Express **11**, 2549-2554 (2003).
7. A. S. Meijer, G. Berden, D. D. Arslanov, M. Ozerov, R. T. Jongma, and W. J. van der Zande, "An ultrawide-bandwidth single-sideband modulator for terahertz frequencies," Nature

Photonics **10**, 740-744 (2016).

8. X. Lu, S. Venkatesh, and H. Saeidi, "A review on applications of integrated terahertz systems," Terahertz Wireless Communications (2021).
9. I. S. Gregory, C. Baker, W. R. Tribe, I. V. Bradley, M. J. Evans, E. H. Linfield, A. G. Davies, and M. Missous, "Optimization of photomixers and antennas for continuous-wave terahertz emission," IEEE Journal of Quantum Electronics **41**, 717-728 (2005).
10. S. Liu, X. Shou, and A. Nahata, "Coherent detection of multiband terahertz radiation using a surface plasmon-polariton based photoconductive antenna," IEEE Transactions on Terahertz Science and Technology **1**, 412-415 (2011).
11. S.-G. Park, K. H. Jin, M. Yi, J. C. Ye, J. Ahn, and K.-H. Jeong, "Enhancement of terahertz pulse emission by optical nanoantenna," ACS Nanophotonics **6**, 2026-2031 (2012).
12. B. Heshmat, H. Pahlevaninezhad, Y. Pang, M. Masnadi-Shirazi, R. Burton Lewis, T. Tiedje, R. Gordon, and T. E. Darcie, "Nanoplasmonic terahertz photoconductive switch on GaAs," Nano Letters **12**, 6255-6259 (2012).
13. S.-G. Park, Y. Choi, Y.-J. Oh, and K.-H. Jeong, "Terahertz photoconductive antenna with metal nanoislands," Optics Express **20**, 25530 (2012).
14. C. W. Berry, N. Wang, M. R. Hashemi, M. Unlu, and M. Jarrahi, "Significant performance enhancement in photoconductive terahertz optoelectronics by incorporating plasmonic contact electrodes," Nature Communications **4**, 1622 (2013).
15. A. Jooshesh, L. Smith, M. Masnadi-Shirazi, V. Bahrami-Yekta, T. Tiedje, T. E. Darcie, and R. Gordon, "Nanoplasmonics enhanced terahertz sources," Optics Express **22**, 27992-28001 (2014).
16. N. M. Burford, M. J. Evans, and M. O. El-Shenawee, "Plasmonic nanodisk thin-film terahertz photoconductive antenna," IEEE Transactions on Terahertz Science and Technology **8**, 237-247 (2018).
17. S. Lepeshov, A. Gorodetsky, A. Krasnok, E. Rafailov, and P. Belov, "Enhancement of terahertz photoconductive antenna operation by optical nanoantennas," Laser & Photonics Reviews **11**(2017).
18. O. Mitrofanov, T. Siday, R. J. Thompson, T. S. Luk, I. Brener, and J. L. Reno, "Efficient photoconductive terahertz detector with all-dielectric optical metasurface," APL Photonics **3**(2018).
19. G. Rana, A. Bhattacharya, A. Gupta, D. Ghindani, R. Jain, S. P. Duttagupta, and S. S. Prabhu, "A polarization-resolved study of nanopatterned photoconductive antenna for enhanced terahertz emission," IEEE Transactions on Terahertz Science and Technology **9**, 193-199 (2019).
20. T. Siday, P. P. Vabishchevich, L. Hale, C. T. Harris, T. S. Luk, J. L. Reno, I. Brener, and O. Mitrofanov, "Terahertz detection with perfectly-absorbing photoconductive metasurface," Nano Letters **19**, 2888-2896 (2019).
21. K. Wang, J. Gu, W. Shi, Y. An, Y. Li, Z. Tian, C. Ouyang, J. Han, and W. Zhang, "All-dielectric nanograting for increasing terahertz radiation power of photoconductive antennas," Opt Express **28**, 19144-19151 (2020).
22. N. Wang, S. Cakmakyapan, Y.-J. Lin, H. Javadi, and M. Jarrahi, "Room-temperature heterodyne terahertz detection with quantum-level sensitivity," Nature Astronomy **3**, 977-982 (2019).

23. D. V. Lavrukhin, A. E. Yachmenev, I. A. Glinskiy, R. A. Khabibullin, Y. G. Goncharov, M. Ryzhii, T. Otsuji, I. E. Spector, M. Shur, M. Skorobogatiy, K. I. Zaytsev, and D. S. Ponomarev, "Terahertz photoconductive emitter with dielectric-embedded high-aspect-ratio plasmonic grating for operation with low- power optical pumps," AIP Advances **9**, 015112 (2019).
24. D. S. Ponomarev, A. Gorodetsky, A. E. Yachmenev, S. S. Pushkarev, R. A. Khabibullin, M. M. Grekhov, K. I. Zaytsev, D. I. Khusyainov, A. M. Buryakov, and E. D. Mishina, "Enhanced terahertz emission from strain-induced InGaAs/InAlAs superlattices," Journal of Applied Physics **125**(2019).
25. A. Singh, M. Welsch, S. Winnerl, M. Helm, and H. Schneider, "Improved electrode design for interdigitated large-area photoconductive terahertz emitters," Optics Express **27**, 13108-13115 (2019).
26. R. B. Kohlhaas, S. Breuer, L. Liebermeister, S. Nellen, M. Deumer, M. Schell, M. P. Semtsiv, W. T. Masselink, and B. Globisch, "637 μW emitted terahertz power from photoconductive antennas based on rhodium doped InGaAs," Applied Physics Letters **117**(2020).
27. K. Takano, Y. Chiyoda, T. Nishida, F. Miyamaru, T. Kawabata, H. Sasaki, M. W. Takeda, and M. Hangyo, "Optical switching of terahertz radiation from meta-atom-loaded photoconductive antennas," Applied Physics Letters **99**(2011).
28. J. F. O'Hara, H.-T. Chen, and A. J. Taylor, "Split-ring resonator enhanced terahertz antenna," Nonlinear Optics: Materials, Fundamentals and Applications (Optical Society of America), TuB2. (2007).
29. Y. Salamin, I. C. Benea-Chelmus, Y. Fedoryshyn, W. Heni, D. L. Elder, L. R. Dalton, J. Faist, and J. Leuthold, "Compact and ultra-efficient broadband plasmonic terahertz field detector," Nature Communications **10**, 5550 (2019).
30. X. Shi, K. Wang, J. Gu, Y. An, R. Jia, Z. Tian, C. Ouyang, J. Han, and W. Zhang, "Photoconductive meta-antenna enabling terahertz amplitude spectrum manipulation," Advanced Photonics Research **2**(2020).
31. K. Lee, S. C. Lee, W. T. Kim, J. Park, B. Min, and F. Rotermund, "Terahertz generation by a resonant photoconductive antenna," Current Optics and Photonics **4**, 373-379 (2020).
32. H. Deng, Z. Xiong, W. Qu, Z. Wu, Q. Liu, L. Chen, J. Guo, and L. Shang, "The impact of structural parameters of split-ring resonators on the terahertz radiation characteristics of micro-structured photoconductive antennas: a simulation study," IEEE Photonics Journal **12**, 1-13 (2020).
33. X. Shen, T. J. Cui, D. Martin-Cano, and F. J. Garcia-Vidal, "Conformal surface plasmons propagating on ultrathin and flexible films," PNAS **110**, 40-45 (2013).
34. D. Woolf, M. A. Kats, and F. Capasso, "Spoof surface plasmon waveguide forces," Optical Letters **39**, 517-520 (2014).
35. F. J. Garcia-Vidal, A. I. Fernández-Domínguez, L. Martin-Moreno, H. C. Zhang, W. Tang, R. Peng, and T. J. Cui, "Spoof surface plasmon photonics," Reviews of Modern Physics **94**(2022).
36. F. Gao, Z. Gao, Y. Luo, and B. Zhang, "Invisibility dips of near-field energy transport in a spoof plasmonic metadimer," Advanced Functional Materials **26**, 8307-8312 (2016).
37. Z. Gao, F. Gao, Y. Zhang, H. Xu, Y. Luo, and B. Zhang, "Forward/Backward switching of

plasmonic wave propagation using sign-reversal coupling," Advanced Materials **29**(2017).

38. Z. Gao, L. Wu, F. Gao, Y. Luo, and B. Zhang, "Spoof plasmonics: from metamaterial concept to topological description," Advanced Materials **30**, e1706683 (2018).
39. S. M. Duffy, S. Verghese, A. McIntosh, A. Jackson, A. C. Gossard, and S. Matsuura, "Accurate modeling of dual dipole and slot elements used with photomixers for coherent terahertz output power," IEEE Transactions on Microwave Theroy and Techniques **49**, 1032-1038 (2001).
40. D. M. Pozar, *Microwave engineering,* Fourth Edition ed. (Wiley, United States of America, 2011).
41. J. D.Joannopoulos, S. G.Johnson, J. N.Winn, and R. D.Meade, *Photonic crystals: modeling the flow of light* (Princeton University Press, Princeton University Press, 2008), Vol. Chapter 1.